Journal of Alloys and Compounds 826 (2020) 154224

Contents lists available at ScienceDirect

Journal of Alloys and Compounds

journal homepage: http://www.elsevier.com/locate/jalcom

A complete computational route to predict reduction of thermal conductivities of complex oxide ceramics by doping: A case study of $La_2Zr_2O_7$

Guoqiang Lan , Pengfei Ou , Cheng Chen , Jun Song *

Department of Mining and Materials Engineering, McGill, University, Montreal, Quebec, H3A 0C5, Canada

ARTICLE INFO

Article history:
Received 3 October 2019
Received in revised form
5 February 2020
Accepted 5 February 2020
Available online 7 February 2020

Keywords:
Zirconate
Pyrochlore
Dopant
Thermal conductivity
Density functional theory

ABSTRACT

Rare-earth (RE) zirconate pyrochlores, of low thermal conductivity and high temperature stability, are widely considered as a candidate material group for thermal barrier coatings (TBCs). Doping of a RE zirconate pyrochlore has been shown to be one possible method towards additional reduction in the thermal conductivity. Focusing on lanthanum zirconate ($La_2Zr_2O_7$) as a representative RE zirconate pyrochlore, we systematically investigated the effect of various doping elements, Gd, Y, Yb, In, Sc, Ce and Hf, on the thermal conductivity. A complete computational route, based on first-principles calculations, to predict the reduction of thermal conductivity by doping, has been developed. Employing first-principles calculations combined with thermodynamic modeling, the defects resulted from doping are explicitly clarified, with their concentrations determined considering the chemical environment. The phonon-defect scattering is then evaluated and the resultant reduction of thermal conductivity is determined from single-mode relaxation-time approximation. Good agreement has been achieved between our model predictions and available experimental data. The present study established a complete computational route, based on first-principles calculations, to predict the reduction of thermal conductivity by doping, not only for RE zirconate pyrochlores, but also for other complex oxide ceramics.

1. Introduction

Thermal barrier coatings (TBCs) are insulating coatings of very low thermal conductivities, deposited on metallic components in high-temperature mechanical systems, such as gas-turbine engines, to enable high gas combustion temperature far beyond the melting point of the metallic component [1–3]. The key component of a TBC that determines its thermal insulating capacity is the ceramic topcoat, typically composed of complex oxide ceramics of low thermal conductivities. The quest for improved performance in advanced gas-turbine engines requires further increase of the operation gas temperature [1–3]. This necessitates technological innovations to design and develop new top coat materials of further reduced thermal conductance.

In recent years, rare-earth (RE) zirconate pyrochlores with a general formula $RE_2Zr_2O_7$ have emerged as promising candidate materials for next-generation TBCs owing to their high-temperature stability [4], and low intrinsic thermal conductivities (i. e., 1–2 $Wm^{-1}K^{-1}$ from room temperature to ~1600 K) [4–7] that are at least 15% lower than the currently used 7 wt% yttria-stabilized zirconia (7YSZ) [4,6]. The remarkably low lattice thermal conductivities of these pyrochlore oxides were reported to originate from their low-lying optical phonon bands [8]. Furthermore, it has been reported that doping on cationic sites can be an effective method to reduce the thermal conductivity of a pyrochlore oxide, e.g., as shown by experiments on doped $La_2Zr_2O_7$ [9–14]. In most of those previous studies [9–12,14], the dopants were assumed to substitute certain cationic sites, i.e., either the RE site or the Zr site in $RE_2Zr_2O_7$. Nonetheless, the above treatment is not accurate for many dopants, which may assume both RE and Zr sites during the substitution process, e.g., Sc and In doping in $La_2Zr_2O_7$ [13]. Moreover, the substitution of both cationic sites can lead to the formation of charge neutralizing defects, i.e., oxygen vacancy or interstitial oxygen. These extra defects introduced by doping can contribute to further lowering the thermal conductivity, which was not considered in previous studies.

Despite the demonstrated effectiveness, an accurate means to quantitatively evaluate the effect of doping on thermal conductivities of pyrochlore oxides is lacking. The doping-induced change in thermal conductivity remains largely assessed by models [15,16] that

* Corresponding author.
E-mail address: jun.song2@mcgill.ca (J. Song).

https://doi.org/10.1016/j.jallcom.2020.154224
0925-8388/

estimate it simply based on basic physical properties measured from experiments [9], with many essential aspects, including, e.g., the site preference by dopants and doping-induced defects, not accounted for. Aiming to address this challenge, in the present work, we propose a systematic computational route to predict the thermal conductivity of doped complex oxides. The $La_2Zr_2O_7$ system doped by the set of elements Gd, Y, Yb, In, Sc, Ce and Hf is selected as the representative study case. Employing first-principles calculations combined with thermodynamic modeling, the preferential doping sites, corresponding substitutional defect concentrations, and the associated oxygen vacancies and interstitials, were determined. First-principles anharmonic lattice dynamics were then applied to evaluate phonon-defect scattering and calculate the lattice thermal conductivity of the doped system. Good agreement between the predicted thermal conductivities and available experimental data was achieved, confirming the accuracy and reliability of our approach.

2. Methodology

2.1. Crystal structure and possible defects

The ideal stoichiometric pyrochlore oxide $A_2B_2O_7$ is cubic (space group $Fd\bar{3}m$) and can be also written as $A_2B_2O_6O'Vac$, with ions A, B, O and O′ occupying sites at 16*d* (1/2, 1/2, 1/2), 16*c* (0, 0, 0), 48*f* (*x*, 1/8, 1/8) and 8*b* (3/8, 3/8, 3/8) respectively, leaving the position 8*a* as vacancy (Vac) [17]. $La_2Zr_2O_7$ (A = La and B=Zr), or LZO is one of the common pyrochlore oxides, which is selected as the representative system of focus for the present study. The main types of defects existing in the LZO doped by element *X* (*X* = Gd, Y, Yb, In, Sc, Ce or Hf) can be substitutional defects, X_h at site *h* (*h* = La or Zr), and the oxygen vacancy (VacO or VacO′) and interstitial oxygen at 8*a* position (O_i). Therefore the general formula for the doped LZO would be $(La_{1-x_1}X_{x_1})_2(Zr_{1-x_2}X_{x_2})_2O_{7-2\zeta+2\eta}$, where x_1 and x_2 denotes the doping concentrations at La and Zr sites respectively, and δ and η are the concentrations of oxygen vacancies and interstitials respectively, per formula unit of $LaZrO_{3.5}$. Note that x_1 and x_2 add up to be the total dopant concentration, denoted as x_0 thereafter. It is worth noting that all of the defects can carry charges but the whole doped system is considered to be charge neutral.

2.2. Basic formalisms

Since the reduction of thermal conductivity is dependent on the defect types which are resulted from dopant, it is necessary to identify the defect types and their corresponding concentrations first, which is hard to do in the experiments. With defect concentrations determined, the thermal conductivities for the doped systems can then be calculated using the single-mode relaxation-time (SMRT) approximation [18] from first-principles anharmonic lattice dynamics calculations. The basic formalisms for calculations of the defect concentrations and the thermal conductivities for doped complex oxides were elaborated in the following.

For the vacancy and interstitial type point defects, the concentration of a defect *D* with charge *q*, is given by Ref. [19].

$$[D^q] = n_D \frac{\exp\left(-\Delta G^f\{D^q\}/k_BT\right)}{1+\sum_{q'}\exp\left(-\Delta G^f\{D^{q'}\}/k_BT\right)}, \quad (1)$$

in which $\Delta G^f\{D^q\}$ represents the formation energy of the defect *D* with charge *q*, n_D is the number of possible sites for the defect *D* in the lattice per formula unit of $LaZrO_{3.5}$ (e.g., $n_{VacO} = 3$, $n_{VacO'} = 0.5$ and $n_{O_i} = 0.5$), k_B is the Boltzmann constant and *T* is the absolute temperature. This equation is used to calculate the concentrations for oxygen vacancies and interstitials.

In the case of a substitutional defect X_h with charge *q*, the defect concentration can be given by

$$\left[X_h^q\right] = \frac{x_0}{\sum_{q'}\sum_{h'}\exp\left(\frac{\Delta G^f\{X_h^q\}-\Delta G^f\{X_{h'}^{q'}\}}{k_BT}\right)} \quad (2)$$

assuming that all the dopants are dissolved into LZO to form a solid solution. In the case of $(La_{1-x_1}X_{x_1})_2(Zr_{1-x_2}X_{x_2})_2O_{7-2\zeta+2\eta}$, we have $x_1 = [X_{La}]$, $x_2 = [X_{Zr}]$, $\zeta = [VacO] + [VacO']$ and $\eta = [O_i]$.

The defect formation energy depends on the difference of the defect induced in the total energy E^{tot} with reference to the pristine system. For an oxygen vacancy with charge *q*, the formation energy is given by Ref. [20].

$$\Delta G^f\{Vac_O^q \text{ or } Vac_{O'}^q\} = E^{tot}\left[n\left(La_2Zr_2O_{7-1/n}\right);q\right] - E^{tot}[n(La_2Zr_2O_7) \times] + \mu_O + q\mu_e, \quad (3)$$

where *n* is the number of $La_2Zr_2O_7$ formula units used in the simulated supercell, μ_O is the chemical potential of oxygen and μ_e is electron chemical potential (or Fermi level). Similarly, for the interstitial oxygen, we have

$$\Delta G^f\left\{O_i^q\right\} = E^{tot}\left[n\left(La_2Zr_2O_{7+1/n}\right);q\right] - E^{tot}[n(La_2Zr_2O_7)] - \mu_O + q\mu_e. \quad (4)$$

The formation energy of a dopant X substituting La- or Zr-site is calculated by Ref. [20].

$$\Delta G^f\{X_{La}^q\} = E^{tot}\left[n\left(La_{2-1/n}X_{1/n}Zr_2O_7\right);q\right] - E^{tot}[n(La_2Zr_2O_7) \times] + \mu_{La} - \mu_X + q\mu_e, \quad (5)$$

and

$$\Delta G^f\{X_{Zr}^q\} = E^{tot}\left[n\left(La_2Zr_{2-1/n}X_{1/n}O_7\right);q\right] - E^{tot}[n(La_2Zr_2O_7) \times] + \mu_{Zr} - \mu_X + q\mu_e, \quad (6)$$

respectively. In the above, μ_{La} and μ_{Zr} are the chemical potentials of the host cations La and Zr respectively, and μ_X is the chemical potential of the substitutional dopant.

The chemical potential of oxygen is calculated as half of Gibbs free energy of one O_2 (gas) molecule, which is [20].

$$\mu_O(T,p) = \frac{1}{2}\left(E_{O_2}^{tot} + E_{O_2}^{corr} + E_{O_2}^{zp} + H_{O_2}\left(T,p^0\right) - TS_{O_2}\left(T,p^0\right) + k_BT\ln\frac{p}{p^0}\right), \quad (7)$$

where $E_{O_2}^{tot}$ is the total energy at 0 K, $E_{O_2}^{zp}$ is the zero-point energy of the oxygen molecule (taken as 0.1 eV here [20]), p^0 is the reference pressure (p^0=1 atm) and p is the partial pressure of the oxygen gas. H_{O_2} and S_{O_2} are the enthalpy and entropy of one oxygen molecule collected from the thermodynamical table [21], respectively. The enthalpy at 0 K, H_{O2} (0, p^0), is set to be zero. $E_{O_2}^{corr}$ is an energy correction term to correct the energy for the oxygen molecule. $E_{O_2}^{corr}$ assumes the values of 0.25 eV and −1.20 eV for Perdew-Zunger local density approximation (PZ-LDA) [22] and Perdew–Burke–Ernzerhof generalized gradient approximation (PBE-GGA) [23] exchange-correlation functionals respectively [24]. Generally we can assume that defects form during sintering. Considering that sintering of LZO is usually occurring at T = 1473–1873 K but with the pressure p unknown [9–14], we chose T = 1473 K (the results calculated at T = 1873 K are not present in this paper since they are very much similar to those at T = 1473 K) and $p = p^0$ as inputs for the defect calculations.

The values of μ_{La} and μ_{Zr}, cannot be exactly pinpointed as they depend on the actual chemical environment. However, their ranges can be determined by considering two limiting cases, i.e., La-rich and Zr-rich situations, which can be taken as the system being in equilibrium with the binary oxides La_2O_3 and ZrO_2 respectively [20]. The maximum value of μ_{La} and minimum value of μ_{Zr} can be determined considering the La-rich case,

$$\mu_{La}^{max} = \mu_{La}^{La_2O_3} = \frac{1}{2}\left(E^{tot}[La_2O_3] - 3\mu_O\right), \tag{8}$$

$$\mu_{Zr}^{min} = \frac{1}{2}\left(E^{tot}[La_2Zr_2O_7] - 2\mu_{La}^{max} - 7\mu_O\right). \tag{9}$$

while similarly the maximum value of μ_{Zr} and minimum value of μ_{La} can be determined considering the Zr-rich case

$$\mu_{Zr}^{max} = \mu_{Zr}^{ZrO_2} = E^{tot}[ZrO_2] - 2\mu_O, \tag{10}$$

$$\mu_{La}^{min} = \frac{1}{2}\left(E^{tot}[La_2Zr_2O_7] - 2\mu_{Zr}^{max} - 7\mu_O\right). \tag{11}$$

It is worth to note that μ_X would be cancelled when plugging Eqs. (5) and (6) into Eq. (2) to calculate the concentrations of substitutional defects. Therefore it is not necessary to calculate μ_X.

For the Fermi level (μ_e), we can pinpoint it by considering charge neutrality of the whole system,

$$\sum_D \sum_q q[D^q] + c_h - c_e = 0, \tag{12}$$

where c_h is the concentration of holes in the valence band, c_e is the concentration of electrons in the conduction band, and the summation is taken over all charged defects. For wide band-gap insulator like LZO (E_{gap} = 3.76 eV in this work and 3.52 eV from measurement [25]), c_h and c_e are negligible comparing to the defect concentrations [19,20] and therefore can be safely omitted. Besides, the band edges, conduction band minimum (ε_{CBM}) and valence band maximum (ε_{VBM}), are obtained according to the work by Nyman et al. [20].

$$\varepsilon_{CBM} = E^{tot}(+1) - E^{tot}(0), \tag{13}$$

$$\varepsilon_{VBM} = E^{tot}(0) - E^{tot}(-1), \tag{14}$$

where $E^{tot}(i)$ represent the total energy of the system with i electron added. And the band-gap energy, E_{gap}, is the difference between ε_{CBM} and ε_{VBM}.

The lattice thermal conductivities were calculated with the single-mode relaxation-time approximation of the linearized phonon Boltzmann transport equation (SMRT-LBTE) from first-principles anharmonic lattice dynamics calculations [18]. For a system with randomly distributed dopants, the virtual crystal approximation (VCA) [16] was used to treat it, where the lattice constants, masses and second-order and third-order interatomic force constants (IFCs) are taken as the weighted averages of $La_2Zr_2O_7$, $X_2Zr_2O_7$ and $La_2X_2O_7$ depending on their molar concentrations. The total phonon scattering rate (reciprocal of total relaxation time) for a phonon mode (λ) is given as the sum of phonon-phonon (PP) and Phonon-dopant (PD) scattering rates,

$$\frac{1}{\tau_\lambda^{tot}} = \frac{1}{\tau_\lambda^{PP}} + \frac{1}{\tau_\lambda^{PD}(\omega_\lambda)}, \tag{15}$$

where ω_λ represents the phonon frequency of the phonon mode λ. The PP scattering rate was calculated using SMRT method [18], while the PD scattering rate is given by the second-order perturbation theory as [18,26].

$$\frac{1}{\tau_\lambda^{PD}(\omega)} = \frac{\pi}{2N}\omega_\lambda^2 \sum_{\lambda'} \delta(\omega - \omega_{\lambda'}) \times \sum_k g_k |\boldsymbol{e}(k,\lambda)\cdot\boldsymbol{e}^*(k,\lambda')|^2, \tag{16}$$

where N is the number of unit cells in the crystal and $\boldsymbol{e}(k, \lambda)$ denote the phonon eigenvector of mode λ for the kth atom and g_k is the variance parameter of the kth atom, which can be defined as [15,16],

$$g_k = \sum_j f_j \left[\left(\frac{\Delta M_{jk}}{\overline{M}_k}\right)^2 + 2\left(\frac{\Delta G_{jk}}{\overline{G}_k} - 6.4\times\gamma_{jk}\frac{\Delta r_{jk}}{\overline{r}_k}\right)^2\right]. \tag{17}$$

In the above expression, we have

$$\overline{P}_k = \sum_j f_j P_{jk}, \tag{18}$$

$$\Delta P_{jk} = P_{jk} - \overline{P}_k, \tag{19}$$

where f_j is the fraction of the element (or defect) j, P_{jk} denotes the atomic property, i.e., mass (M), radius (r) or local stiffness (G) of the element (or defect) j at the kth atomic site, and γ_{jk} denotes the Grüneisen parameter (i.e., anharmonicity) for the element (or defect) j at the kth atomic site. In addition, the detailed procedures to calculate r_{jk}, G_{jk} and γ_{jk} for a cation can be found in the Supplementary information.

With the scattering rates determined (cf. Eqs. (15) and (16)), the thermal conductivity can then be calculated based on SMRT-LBTE, given by Ref. [18],

$$\kappa_{\alpha\beta} = \frac{1}{NV_0}\sum_\lambda C_\lambda v_\lambda^\alpha v_\lambda^\beta \tau_\lambda^{tot}, \tag{20}$$

where V_0 is the volume of a unit cell, C_λ and v_λ are the heat capacity and group velocity of the phonon mode λ, respectively, which can be obtained from the phonon frequency ω_λ and second-order IFCs [18]. α, β and γ represent the Cartesian indices.

2.3. First-principles calculations

The relevant structural and energetic values were obtained from the first-principles spin-polarized density functional theory (DFT) calculations, which were performed using the Vienna ab initio simulation package (VASP) [27,28] with Perdew-Zunger local

Table 1
The elements involved in this study with their corresponding valence states treated within the PAW pseudopotentials and Hubbard U values for dopant at A-site (U_A) and B-site (U_B) determined from LRA. The $\overline{U}$ is the average values calculated from U_A and U_B, which is used for all defect energy calculations. The U_A and U_B are adopted in all structural optimizations and phonon calculations. Note that all U corrections are applied on the d-orbitals of the elements except for Ce, whose f-orbital is chosen to be corrected. The pseudopotential used for Yb has been treated in VASP and hence U correction is not necessary.

Element	Valence state	U_A (eV)	U_B (eV)	$\overline{U}$ (eV)
Gd	$5p^6\ 5d^1\ 6s^2$	0.92	0.62	0.77
Y	$4s^2\ 4p^6\ 5d^1\ 5s^2$	3.01	1.84	2.43
Yb	$5p^6\ 4f^1\ 6s^2$	–	–	–
In	$5s^2\ 5p^1$	–	–	–
Sc	$3s^2\ 3p^6\ 3d^1\ 3s^2$	2.43	1.60	2.02
Ce	$5p^6\ 4f^1\ 5d^1\ 6s^2$	5.88	4.96	5.42
Hf	$5s^2\ 5p^6\ 5d^2\ 6s^2$	3.08	2.39	2.74
La	$5s^2\ 5p^6\ 5d^1\ 6s^2$	1.67	–	–
Zr	$4s^2\ 4p^6\ 4d^2\ 5s^2$	–	2.21	–
O	$2s^2\ 2p^4$	–	–	–

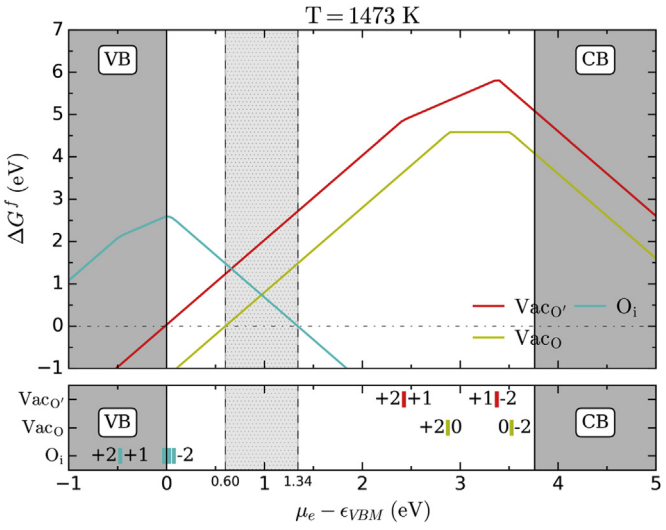

Fig. 1. Calculated formation energies of oxygen vacancies, i.e., Vac_O and $Vac_{O'}$, and interstitial oxygen i.e., O_i, respectively denoted as yellow, red and cyan curves, as functions of the electron chemical potential (top panel) and corresponding charge transition levels (bottom panel). Note that for a defect at any particular chemical potential, only the lowest formation energy value (and the most stable charge state) is shown. The valence band and conduction band are denoted as grey shadows with text 'VB' and 'CB' respectively. The dotted shadow represents the valid range of electron chemical potential where defects exhibit positive formation energies. (For interpretation of the references to color in this figure legend, the reader is referred to the Web version of this article.)

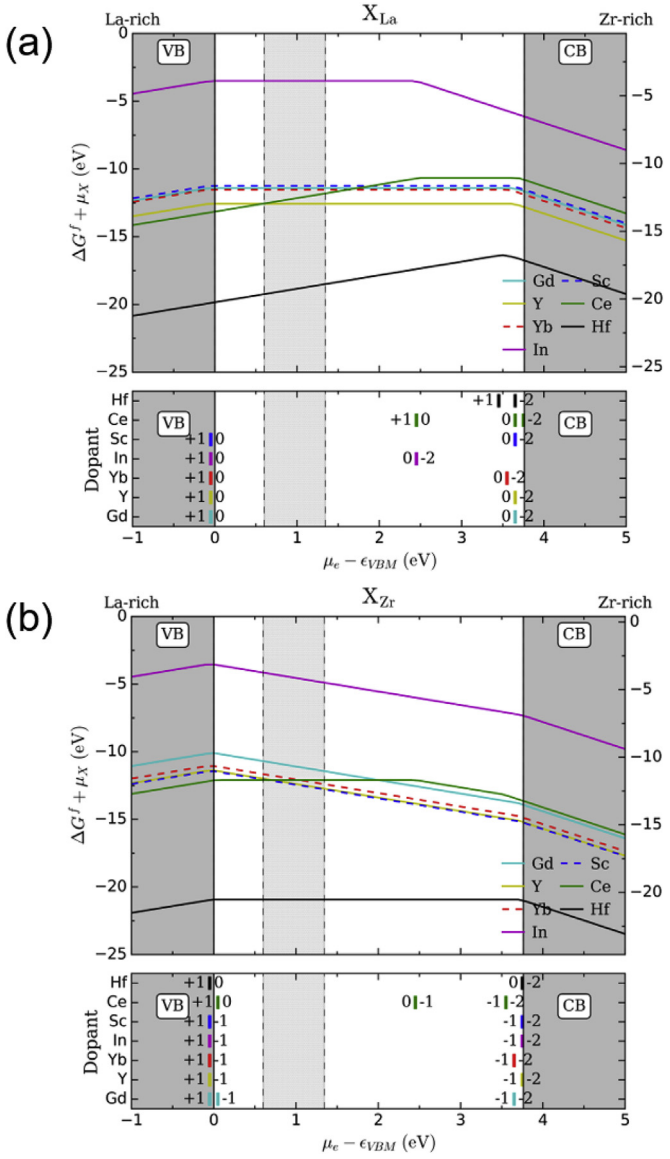

Fig. 2. (top panel) DFT calculated formation energies (with respect to the chemical potential of dopant μ_X, at 1473K), $\Delta G^f + \mu_X$ as functions of the electron chemical potential and (bottom panel) corresponding charge transition levels for a set of substitutional dopants i.e., Y (yellow), Gd (cyan), Yb (red), Sc (blue), In (purple), Ce (green) and Hf (black), located at (a) La- and (b) Zr-site. For each defect only the most stable charge states are shown. Left and right energy scale represent energies are calculated in La-rich (cf. Eqs. (8) and (9)) and Zr-rich (cf. Eqs. (10) and (11)) conditions respectively. The valence band and conduction band are denoted as grey shadows with text 'VB' and 'CB' respectively. The dotted shadow region represents the valid range of electron chemical potential where all the defects exhibit positive formation energies. (For interpretation of the references to color in this figure legend, the reader is referred to the Web version of this article.)

density approximation (PZ-LDA) [22] based on plane-wave basis sets. The electron–core interaction was described by the Blöchl's projector augmented wave method (PAW) within the frozen-core approximation [29]. For the systems having transition metal elements or lanthanides, DFT + U (in this study, LDA + U, see below) are also necessary to be used to enhance the on-site Coulomb interactions, which is underestimated in the DFT [30]. A linear response approach (LRA) has been proposed to determine the Hubbard U values internally instead of empirically [31,32]. It has been proved in our previous work [32] that U values determined from LRA can improve the predictions of key thermophysical properties for the pyrochlore oxides. Hence, in this study we adopt the LDA + U approach as well. It is worth noting that in our DFT calculations, LDA + U is used instead of GGA + U, as it provides much better agreement (in thermal conductivity predictions) with the experiments. The valence configurations of the elements and the corresponding U values determined from LRA are shown in Table 1. Lattice parameters are optimized using the pyrochlore primitive cell (22 atoms) with a 2×2×2 Monkhorst-Pack (MP) k–mesh for Brillouin-zone integration, a cutoff energy of 520 eV for the plane-wave basis set, and a convergence criteria of 10^{-9} eV and 10^{-6} eV Å^{-1} for the total energy and the force respectively on each ion. All defect calculations were performed using 2×2×2 periodic supercell constructed from primitive cell with 1×1×1 Monkhorst-Pack (MP) k–mesh. Point defects carrying charge were modeled by

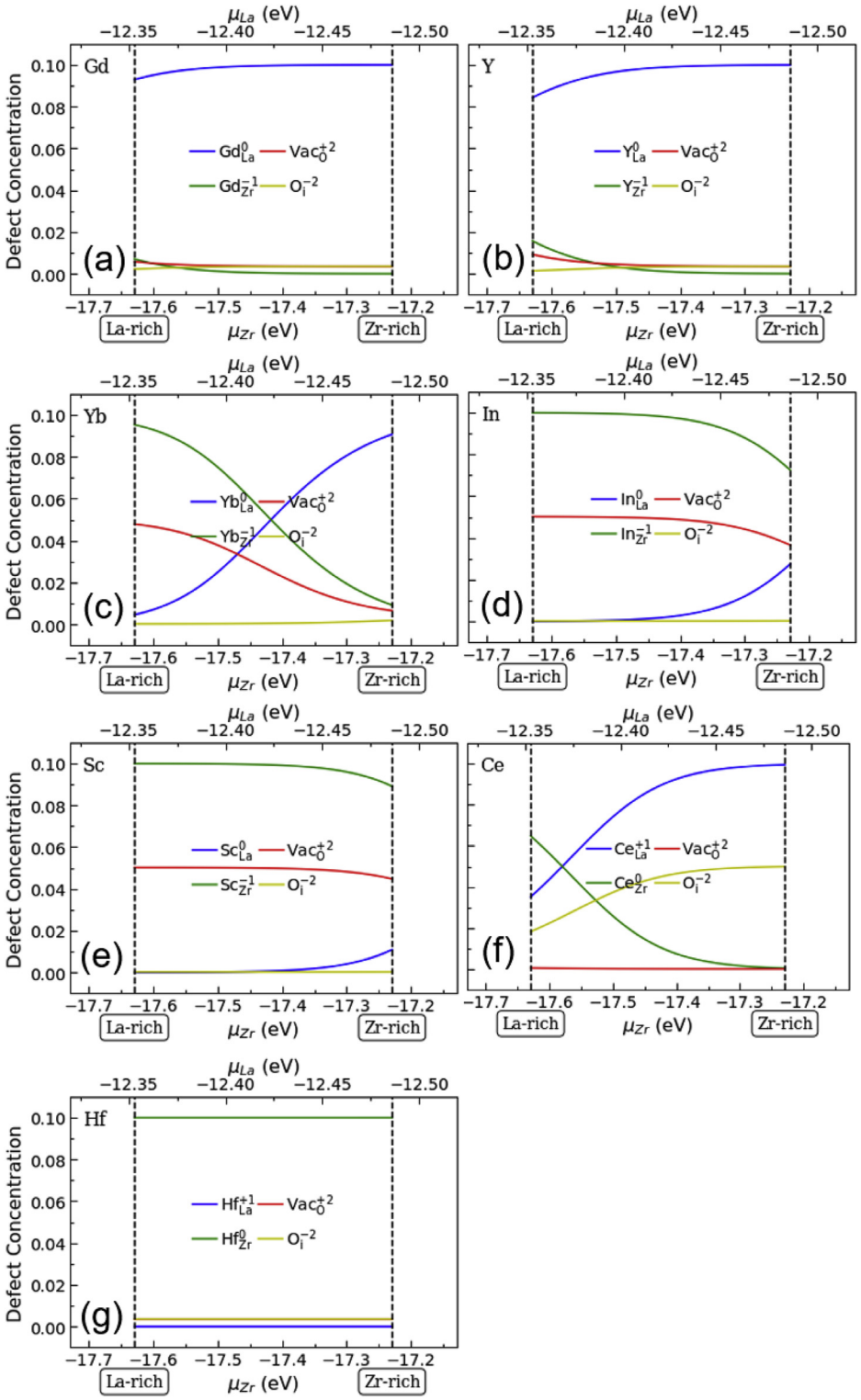

Fig. 3. (color online) The defect concentrations as functions of μ_{Zr} (or μ_{La}) at T = 1473 K, $p = p^0$ and $x_0 = 0.1$ for LZO doped by (a) Gd, (b) Y, (c) Yb, (d) In, (e) Sc, (f) Ce and (g) Hf. The blue, green, red and yellow curves denote the X_{La}, X_{Zr}, Vac_O and O_i defects respectively. (For interpretation of the references to color in this figure legend, the reader is referred to the Web version of this article.)

modifying the number of electrons in the supercell in terms of the charge carried. Band gap and band edges (CBM, VBM) were obtained using Eqs. (12) and (13). For LZO, the band gap from our calculations is 3.76 eV, in good agreement with the experimental measurement, 3.52 eV [25].

PHONOPY [33,34] and PHONO3PY [18] were used for the phonon and heat-transport calculations. The second- and third-order IFC were obtained with the finite-displacement supercell method [35] using 2×2×2 periodic supercells constructed from the pyrochlore primitive cell with a 1×1×1 MP *k*—mesh as well. For calculations of

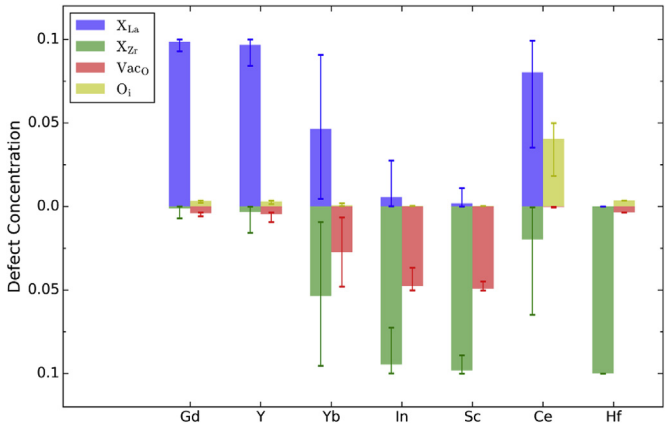

Fig. 4. (color online) The average defect concentration $\overline{[D]}$ (cf. Eq. (20)), calculated at $T = 1473$ K, $p = p^0$ and $x_0 = 0.1$ for LZO doped by Gd, Y, Yb, In, Sc, In, Ce and Hf. The blue, green, red and yellow bars correspond to X_{La}, X_{Zr}, Vac_O and O_i defects respectively. The lower and upper limit of the error bars denote the defect concentrations at La- and Zr-rich conditions respectively. (For interpretation of the references to color in this figure legend, the reader is referred to the Web version of this article.)

thermal conductivity, the 9×9×9 **q**-mesh was applied considering accuracy and computational cost. The detail procedures to select the **q**-mesh can be found in the Supplementary information.

3. Results and discussion

3.1. Defect formation energetics

3.1.1. Oxygen defect

Using Eqs. (3), (4) and (7), the formation energies of oxygen defects, i.e., O (48*f*) and O' (8*b*) vacancies and interstitial O (8*a*), were calculated for charges $q = +2, +1, 0, -1, -2$. As aforementioned in Section 2.2, defect formation was evaluated at $T = 1473$K, a typical sintering temperature for LZO. Fig. 1 show the formation energies as a function of the electron chemical potential and corresponding charge transition levels for the oxygen defects (Vac_O, $Vac_{O'}$, O_i) at 1473 K (typical sintering temperature, see previous description in Section 2.2). Note that for each of the defect only the charge state with lowest formation energies (i.e., the most stable charge state) were shown. For both of the oxygen vacancies ($Vac_{O'}$ and Vac_O), it is seen that the +2 charge state is the most stable over the majority portion of the band gap. The formation energy of Vac_O is significantly (about 1 eV) lower than that of VacO′, indicating that almost all of the oxygen vacancies form at O (48f) instead of O' (8b) positions. For the interstitial O (O_i) defect, the −2 charge state is the most stable (exhibiting much lower energy than the other states) over the band gap. It is important to note that the negative charge (−2) coming from O_i is crucial to neutralize the system consisting Vac_O and/or substitutional defects carrying positive charges. In addition, all oxygen defects ought to exhibit positive formation energies, as otherwise the pyrochlore structure would not be stable. Consequently this renders the valid range of electron chemical potential where all defect formation energies are positive, which corresponds to the range of (μ_e - ε_{VBM}) being between 0.60 and 1.34 eV, as indicated by the dotted shadow in Fig. 1.

3.1.2. Substitutional dopants

The formation energies with chemical potential of dopant ($\Delta G^f + \mu_X$) as a function of the electron chemical potential (cf. Eqs. (4-5) and (9-11)) and corresponding charge transition levels for a set of substitutional dopants (i.e., Y, Gd, Yb, Sc, In, Ce and Hf) on La- and Zr-site calculated at T = 1473 K are show in Fig. 2 (a) and (b) respectively. We see that the transition levels of charge state for all these dopants located around the band edges, except for In (at La site) and Ce (at La and Zr sites), which may exhibit one additional charge state at the electron chemical potential of ~2.5 eV, attributing to the larger electronegativity of In and Ce retaining one electron localized at its 4*f* orbital. Nonetheless, within the valid range of electron chemical potential (as indicated by the dotted shadow), all these dopants exhibit their common oxidation states, corresponding to Y_{La}^0, Gd_{La}^0, Yb_{La}^0, Sc_{La}^0 In_{La}^0 Ce_{La}^{+1}, Hf_{La}^{+1} and Y_{Zr}^{-1}, Gd_{Zr}^{-1}, Yb_{Zr}^{-1}, Sc_{Zr}^{-1}, In_{Zr}^{-1}, Ce_{Zr}^0, Hf_{Zr}^0 substitutional defects at La-site (X_{La}) and Zr-site (X_{Zr}) respectively. We found that the formation energy of X_{La} (X_{Zr}) calculated under La-rich condition (with μ_{La}^{max} and μ_{Zr}^{min}, cf. Eqs. (8) and (9)) is (~0.4 eV) higher (lower) than that calculated at Zr-rich condition (with μ_{La}^{min} and μ_{Zr}^{max}, cf. Eqs. (10) and (11)) (cf. Fig. 2 (a) and Fig. 2 (b) for the X_{La} and X_{Zr} respectively). In other words, La-rich and Zr-rich condition facilitates formation of the X_{Zr} and X_{La} substitutional defects respectively.

3.2. Defect concentration and lattice constant upon doping

Plugging the defect formation energies into Eqs. (1) and (2), we can obtain the concentrations of oxygen (Vac_O, $Vac_{O'}$ and O_i) and substitutional (X_{La}, X_{Zr}) defects of different charge states. For a certain temperature (T), total dopant concentration (x_0) and oxygen partial pressure (p), the concentrations of oxygen defects are functions of μ_e, while those of substitutional defects are functions of μ_e and μ_{Zr} (or μ_{La}). For the three parameters, μ_e, μ_{Zr} and μ_{La}, μ_{Zr} and μ_{La} take values in the ranges between La-rich and Zr-rich conditions defined by Eqs. (8)–(11), while μ_e can be pinpointed from the charge neutral condition, i.e., by plugging all the defect concentrations into Eq. (12). Fig. 3 shows the defect concentrations as a functions of μ_{Zr} (or μ_{La}) at T = 1473 K, $p = p^0$ and $x_0 = 0.1$ for LZO doped by Gd, Y, Yb, In, Sc, In, Ce and Hf. Note that only the concentrations of Vac_O^{2+}, O_i^{2-} and the substitutional defects with dopants being in common oxidation states are shown since they are the prevailing types of defects in the system (i.e., their concentrations are orders of magnitude higher than other defects). The increase or decrease of μ_{Zr} results in enhanced or decreased concentration of the X_{La} defect respectively, while the increase or decrease of μ_{La} facilitates or discourages substitution at the Zr site respectively. Particularly for the seven doping elements considered, Gd and Y predominately prefer substitution at the La site, while on the contrary, Hf, Sc and In strongly prefer substitution at the Zr site, *albeit* that In may exhibit notable doping at the La site at high μ_{Zr} (or low μ_{La}). On the other hand, the dopants Yb and Ce show alternating site preference depending μ_{Zr} (or μ_{La}), with Zr site and La site doping preferred under La-rich and Zr-rich conditions respectively. Meanwhile, we can see from Fig. 3 that the concentrations of Vac_O^{2+} and O_i^{2-} are generally small. However, in the situations of high X_{Zr}^{-1} (e.g., In_{Zr}^{-1} in Fig. 3d) or X_{La}^{+1}(e.g., Ce_{La}^{+1}) presence, the concentration of Vac_O^{2+} or O_i^{2-} respectively will increase accordingly as the comitant charge-neutralizing agent.

As clearly demonstrated by Fig. 3, the defect concentration is dependent on μ_{Zr} (or μ_{La}). However, because the exact values of μ_{Zr} (or μ_{La}) would depend on the actual synthesis condition and cannot be precisely pinpointed, therefore the resultant defect concentration may vary. Considering such indeterminacy, in this work we calculated the average defect concentration, defined as

$$\overline{[D]} = \int_{\mu_{Zr}^{min}}^{\mu_{Zr}^{max}} [D] d\mu_{Zr} \Big/ \left(\mu_{Zr}^{max} - \mu_{Zr}^{min}\right), \tag{21}$$

where $D = X_{La}$, X_{Zr}, Vac_O and O_i, representing the defect type. Fig. 4

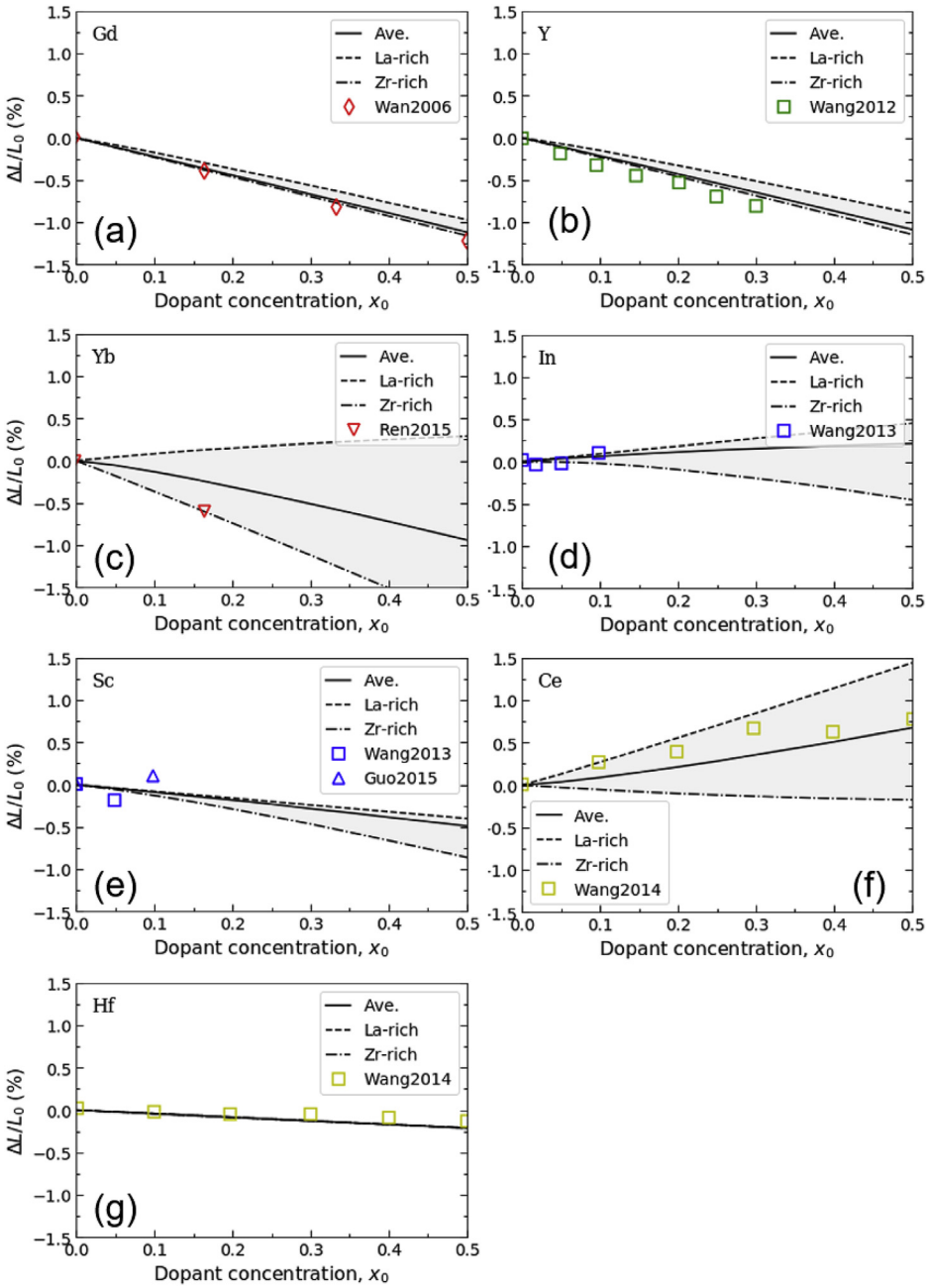

Fig. 5. (color online) The doping-induced lattice constant change ratio, $\Delta L/L_0$, as a function of the total dopant concentration x_0, for LZO doped by (a) Gd, (b) Y, (c) Yb, (d) In, (e) Sc, (f) Ce and (g) Hf calculated at $T = 1473$ K and $p = p^0$. The solid, dashed and dashed-dotted lines respectively denote the $\Delta L/L_0$ calculated using the average defect concentration, and defect concentrations corresponding to the La- and Zr-rich limits. The calculated results are compared with various experimental measurements (i.e., Wan2006 [9], Wang2012 [10], Ren2015 [11], Wang2013 [13] and Wang2014 [14]), which are indicated by open symbols. (For interpretation of the references to color in this figure legend, the reader is referred to the Web version of this article.)

shows the calculated values of $\overline{[D]}$ for doping at Zr and La sites (top panel) and associated Vac_O and O_i defects (bottom panel). In the sequence of Gd, Y, Yb, In and Sc, the average concentration of X_{Zr} and Vac_O defects increase, while in contrast the average concentration of X_{La} decreases, with the amount of O_i stays negligible. Dopant Ce can substitute both of the Zr- and La-site with formation of considerable amount of O_i defect, while Hf would only occupy the Zr-site. In addition, we can see from the error bars that large variation in the defect concentration would be expected for the cases of Yb and Ce doping of LZO.

Meanwhile, with the defect concentration determined, we can further estimate the resultant lattice constant of the doped LZO:

$$L(x_0) = (1 - x_0)L_0 + x_1 L_{X_2Zr_2O_7} + x_2 L_{La_2X_2O_7} \tag{22}$$

where L_0 and $L(x_0)$ denoted the lattice constants of the pristine and doped LZO of a total dopant concentration x_0 respectively, $L_{X_2Zr_2O_7}$ and $L_{La_2X_2O_7}$ denote the lattice constants corresponding to full dopant substitution at the La and Zr sites respectively, and $x_1 = [X_{La}]$ and $x_2 = [X_{Zr}]$ are actual doping concentrations at La and Zr sites respectively. As mentioned above, the values of x_1 and x_2 are

Table 2
Calculated values of ionic radius, r_X (Å), stiffness, G_X (eV/Å^2) and Grüneisen parameters, γ_X, for the dopant X located at A-site and B-site, and the atomic mass, M_X (AMU).

Dopant X	r_X		G_X		γ_X		M_X
	A	B	A	B	A	B	
Gd	1.16	0.85	10.54	9.62	1.99	1.58	157.25
Y	1.16	0.84	10.94	9.51	1.82	2.83	88.91
Yb	1.10	0.79	8.95	10.33	2.64	1.71	173.05
In	1.11	0.80	9.94	13.96	6.02	1.91	114.82
Sc	1.07	0.74	6.81	8.60	4.16	1.99	44.96
Ce	1.22	0.83	10.83	17.01	1.77	2.21	140.12
Hf	0.93	0.71	14.57	20.63	3.44	1.65	178.49
La	1.23	–	11.19	–	1.70	–	138.90
Zr	–	0.72	–	18.75	–	1.70	91.22

dependent on μ_{Zr} (or μ_{La}) and cannot be precisely pinpointed. In this regard, here we computed $L(x_0)$ using the defect concentrations calculated at two limit cases, i.e., La- and Zr-rich conditions, as well as the average defect concentration. In Fig. 5, we compared the doping induced lattice constant change ratio, defined as $\Delta L/\ L_0 = [L(x_0) - L_0]/L_0$, as a function of the total dopant concentration x_0, with available experimental data [9–11,13,14], for different doped systems. Despite the limited experimental data, overall we can see good agreement between our prediction and experimental measurements, with most experimental data falling into or staying close to the range set by the La- and Zr-rich limits except the system doped by Sc, for which the experimental measurements show some scattering yet the deviation is still reasonably small. The good agreement evinces the validity and accuracy of our theoretical approach.

Moreover, one thing worth noting is that the comparison between theoretical predictions and experimental data in Fig. 5 can also provide hints on the chemical environment for experiments. For instance, for the systems doped by Gd, Y and Yb, the experimental data [9–11] are located close to the lower boundary of prediction (i.e., Zr-rich limit), thus indicative of synthesis under the Zr-rich condition. For dopant Ce, the experimental data are located close to the La-rich limit initially but approach the average case (i.e., solid line) for higher x_0 values, suggesting a varying chemical environment for experiments.

3.3. Effect of doping on lattice thermal conductivity of LZO

As elaborated above (cf. Eqs. (15)–(20)), the effect of doping on thermal conductivity can be evaluated by examining the phonon scattering rate, reflected in the PD scattering rate. According to Eqs. (16) and (17), the PD scattering rate increases with the variance parameter that is dependent on the defect concentration, atomic mass, ionic radius, stiffness and Grüneisen parameter. Table 2 shows the calculated values of ionic radius (r_X), stiffness (G_X) and Grüneisen parameter (γ_X) for dopant X located at A-site and B-site along with the atomic mass (M_X). We see that the values of r_X, G_X and γ_X can be site-dependent. Using these atomic properties as inputs, we can compute the variance parameter g_X (cf. Eq. (17)). Meanwhile, from Eq. (17) above, we see that the g_x parameter essentially gets contributions from variation in mass, stiffness and size, in light of which we can also define $g_X^{MV} = \sum f_j(\Delta M_{jX}/\overline{M}_X)^2$, $g_X^{GV} = \sum f_j[2(\Delta G_{jX}/\overline{G}_X)^2]$ and $g_X^{SV} = \sum f_j[2(6.4\times\gamma_{jX}^i\Delta r_{jX}/\overline{r}_X)^2]$ to separately examine the mass, stiffness and size variance contributions. It is, however, worth noting that g_x is not a simple summation of those individual variance contributions. Table 3 shows some sample values of g_X, g_X^{MV}, g_X^{GV} and g_X^{SV} calculated for the X_{La}, X_{Zr} and Vac_O defects (in $(La_{1-x_1}X_{x_1})_2(Zr_{1-x_2}X_{x_2})_2O_{7-2\zeta+2\eta}$) with their concentrations being $x_1 = 0.1$, $x_2 = 0.1$ and $\zeta = 0.05$ respectively. As illustrated in Table 3, for the substitutional defects (i.e., X_{La} and X_{Zr}), g_X^{SV} is the most dominant factor in contribution to the variance parameter, thus subsequently the scattering rate and reduction of κ. However, there is one exception, being Hf doping at the Zr site, for which the g_X^{MV} is more important. This is, however, expected because of the small size difference between Hf and Zr cations (see Table 2). On the other hand, g_X^{GV} is generally very small for the substitutional defects but plays a significant role for the oxygen vacancy (Vac_O). In addition, overall we see that the substitutional defect exhibits considerably larger variance parameter than that from the oxygen vacancy, and therefore is expected to much more effective in affecting κ of the material.

As afore-described, with the variance parameters of defects, along with their concentrations, determined, the phonon scattering rate of a doped LZO can be evaluated (cf. Eqs. (15) and (16)). Subsequently the thermal conductivity κ of a doped LZO can be obtained (cf. Eq. (20)). Fig. 6 shows the predicted change in the thermal conductivity with reference to the pristine LZO, i.e., $\Delta\kappa = \kappa - \kappa_{LZO}$, as a function of the total dopant concentration, x_0, for LZO doped by Gd, Y, Yb, In, Sc, In, Ce and Hf calculated at $T = 473$ K, in comparison with available experimental data [7,9–11,13,36]. As seen in Fig. 6, the La-rich and Zr-rich conditions provide the bounds of the predicted $\Delta\kappa$, while the average condition (i.e., based on the average defect concentrations) gives the intermediate prediction. We see that overall most of the experimental measurements (despite limited availability) fall into or close to the range of predictions bounded by La- and Zr-rich limits. However, we can note that for the case of Gd-doped LZO, there exists sizable deviation between prediction and some experimental data. In particular, we see from Fig. 6a that our prediction shows good agreement with the experimental $\Delta\kappa$ data from the studies by Lehmann et al. [7] and Pan et al. [36], but are considerably lower than those reported in experiments by Wan et al. [9]. Nonetheless, a careful examination of the work of Wan et al. [9] revealed that their thermal conductivity data are consistently higher than those from a more recent work, i.e., Pan et al. [36], from the same research group. For instance, Wan et al. [9] reported an intrinsic thermal conductivity

Table 3
Calculated size variance (g_X^{SV}), stiffness variance (g_X^{GV}), mass variance (g_X^{MV}) and total variance (g_X) for X_{La}, X_{Zr} and Vac_O defects in $(La_{1-x_1}X_{x_1})_2(Zr_{1-x_2}X_{x_2})_2O_{7-2\zeta+2\eta}$ with their concentrations being $x_1 = 0.1$, $x_2 = 0.1$ and $\zeta = 0.05$, respectively.

Dopant X	X_{La}, $x_1 = 0.1$				X_{Zr}, $x_2 = 0.1$				VacO, $\zeta = 0.05$			
	g_X^{SV}	g_X^{GV}	g_X^{MV}	g_X	g_X^{SV}	g_X^{GV}	g_X^{MV}	g_X	g_X^{SV}	g_X^{GV}	g_X^{MV}	g_X
Gd	0.090	0.001	0.002	0.077	0.581	0.047	0.041	1.000	0.000	0.034	0.017	0.051
Y	0.072	0.000	0.013	0.079	1.543	0.048	0.000	2.133	0.000	0.034	0.017	0.051
Yb	0.495	0.007	0.005	0.386	0.206	0.040	0.061	0.488	0.000	0.034	0.017	0.051
In	2.405	0.002	0.003	2.266	0.297	0.012	0.006	0.436	0.000	0.034	0.017	0.051
Sc	1.906	0.030	0.047	1.514	0.031	0.059	0.026	0.200	0.000	0.034	0.017	0.051
Ce	0.001	0.000	0.000	0.000	0.823	0.002	0.023	0.919	0.000	0.034	0.017	0.051
Hf	5.062	0.015	0.007	5.637	0.008	0.002	0.069	0.086	0.000	0.034	0.017	0.051

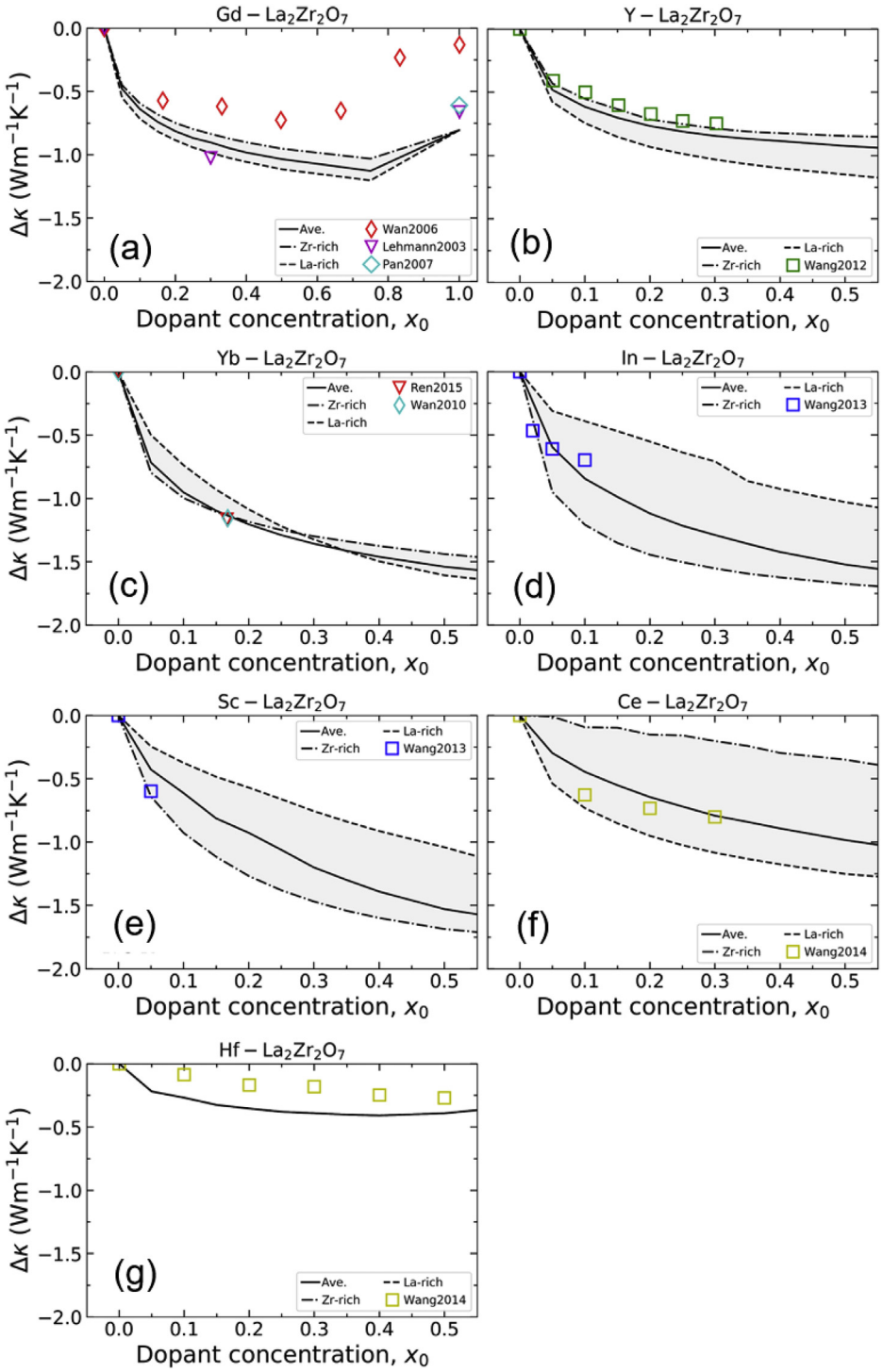

Fig. 6. (color online) The relative lattice thermal conductivity ($\Delta\kappa = \kappa - \kappa_{LZO}$) with respect to the total dopant concentration, x_0, for the LZO doped by Gd, Y, Yb, In, Sc, In, Ce and Hf calculated at $T = 473$ K. The κ calculated according to average defect concentrations are denoted as solid lines. The dashed and dashed-dotted lines represent the calculations performed at La- and Zr-rich limits respectively. The scopes of predictions bounded by La- and Zr-rich limit are filled with grey shade. The calculated results are compared with various experimental measurements (i.e., Lehmann2003 [7], Wan2006 [9], Wang2012 [10], Ren2015 [11] Wan2010 [12], Wang2013 [13] and Wang2014 [14], Pan2007 [36]). (For interpretation of the references to color in this figure legend, the reader is referred to the Web version of this article.)

of ~2.0 $Wm^{-1}K^{-1}$ for pristine $Gd_2Zr_2O_7$ (at $T = 473$ K), while the later work, Pan et al. [36], reported a much lower value of κ = ~1.3 $Wm^{-1}K^{-1}$ (which is very close to our prediction, 1.24 $Wm^{-1}K^{-1}$). Therefore we believe the deviation seen in Fig. 6a is very likely resulted from uncertainty in experimental measurements. Meanwhile, comparing the resultant reduction from different dopants, we see that on average, Yb, In and Sc are all quite effective in reducing thermal conductivity, yet In and Sc show wider $\Delta\kappa$ ranges, and thus their actual effectiveness may vary depending on the chemical environment. On the other hand, we see Hf is the least

effective one among all dopants considered. This can be attributed to the small variance parameter (g_X) for Hf substituting the Zr site (the predominant site Hf occupies, see Fig. 3g regardless of the chemical environment), as demonstrated in Table 3.

From the above results, we see that overall for doping as a method to reduce the thermal conductivity of a complex oxide, its effectiveness not only depends on the dopant type, but also the chemical environment (cf. Fig. 6). The reduction in thermal conductivity by a doping element may be maximized by tuning the chemical environment to drive dopants towards to the substitutional sites that would result in larger variance parameters. It is important to note that the results in Fig. 6 correspond to temperature $T = 473$K, which is chosen because rich experimental data are available at 473K and the radiation contribution on thermal conductivity can be ignored at such low temperature. This temperature is not to be confused with the typical sintering temperature of 1473K used in the calculations of defect concentrations. Moreover, it is worth noting that in our study we assume no doping-induced changes in the lattice (pyrochlore) structure for simplicity, while in reality one needs to take caution in respecting the solubility limits of in the pyrochlore phase, as excessive doping would result in complications such as precipitation and phase transformation, which are not considered in our computational approach. Hence, we only compare our calculated results with the experimental ones measured in pyrochlore phase. In addition, besides the defects considered in the present study, it also worth noting that there exist other intrinsic defects, such as Frenkel and Schottky disorders, which may also contribute to influencing thermal conductivity, particularly at high temperatures. Those complications are beyond the scope of the present work but certainly warrant further studies.

4. Conclusion

To conclude, we conducted a comprehensive first-principles investigation of the effect of doping on thermal conductivity of RE zirconate pyrochlores, using $La_2Zr_2O_7$ doped by Gd, Y, Yb, In, Sc, Ce and Hf as a representative model system. Different defects resulted from doping, including dopant substitution at La and Zr sites, charge neutralized oxygen vacancies and oxygen interstitials, were identified and examined, with the defect concentration quantitatively evaluated as the chemical environment varies. With the defect concentrations obtained, the phonon-defect scattering rates and subsequently the doping induced reduction of thermal conductivity can be quantitatively evaluated from single-mode relaxation-time approximation. The comparison between our predictions of thermal conductivity and available experimental data shows good agreement, confirming the accuracy of our approach. As an additional note, it is worth mentioning that in other systems, there may be need to consider other defect types, e.g., cationic interstitials in systems of small cations, which can be a topic for future studies.

The present study demonstrated a systematic computational route to quantitatively assess the reduction of thermal conductivity resulted from doping in RE zirconate pyrochlores. The approach is also expected to be generally applicable for other complex oxide ceramics. Our findings provide new quantitative predictive tools towards efficient screening and exploring of TBC materials.

Declaration of competing interest

The authors declare that they have no known competing financial interests or personal relationships that could have appeared to influence the work reported in this paper.

CRediT authorship contribution statement

Guoqiang Lan: Conceptualization, Methodology, Software, Investigation, Formal analysis, Visualization, Writing - original draft, Formal analysis. **Pengfei Ou:** Investigation, Formal analysis. **Cheng Chen:** Investigation, Formal analysis. **Jun Song:** Conceptualization, Supervision, Project administration, Funding acquisition, Writing - review & editing.

Acknowledgement

We greatly thank the financial support from McGill Engineering Doctoral Award, National Sciences and Engineering Research Council (NSERC), Consortium for Research and Innovation in Aerospace in Québec (CRIAQ), Aerospace Research and Innovation in Canada (CARIC) and Pratt & Whitney Canada. We also acknowledge Supercomputer Consortium Laval UQAM McGill and Eastern Quebec for providing computing power.

Appendix A. Supplementary data

Supplementary data to this article can be found online at https://doi.org/10.1016/j.jallcom.2020.154224.

References

[1] B. Gleeson, Thermal barrier coatings for aeroengine applications, J. Propul. Power 22 (2) (2006) 375–383.
[2] D.R. Clarke, C.G. Levi, Materials design for the next generation thermal barrier coatings, Annu. Rev. Mater. Res. 33 (1) (2003) 383–417.
[3] A.G. Evans, D.R. Clarke, C.G. Levi, The influence of oxides on the performance of advanced gas turbines, J. Eur. Ceram. Soc. 28 (7) (2008) 1405–1419.
[4] C.G. Levi, Emerging materials and processes for thermal barrier systems, Curr. Opin. Solid State Mater. Sci. 8 (1) (2004) 77–91.
[5] G. Suresh, G. Seenivasan, M.V. Krishnaiah, P. Srirama Murti, Investigation of the thermal conductivity of selected compounds of gadolinium and lanthanum, J. Nucl. Mater. 249 (2–3) (1997) 259–261.
[6] J. Wu, X. Wei, N.P. Padture, P.G. Klemens, M. Gell, E. García, P. Miranzo, M.I. Osendi, Low-thermal-conductivity rare-earth zirconates for potential thermal-barrier-coating applications, J. Am. Ceram. Soc. 85 (12) (2002) 3031–3035.
[7] H. Lehmann, D. Pitzer, G. Pracht, R. Vassen, D. Stöver, Thermal conductivity and thermal expansion coefficients of the lanthanum rare-earth-element zirconate system, J. Am. Ceram. Soc. 86 (8) (2003) 1338–1344.
[8] G. Lan, B. Ouyang, J. Song, The role of low-lying optical phonons in lattice thermal conductance of rare-earth pyrochlores: a first-principle study, Acta Mater. 91 (2015) 304–317, 0.
[9] C.L. Wan, W. Pan, Q. Xu, Y.X. Qin, J.D. Wang, Z.X. Qu, M.H. Fang, Effect of point defects on the thermal transport properties of (LaxGd1-x)2Zr2O7: experiment and theoretical model, Phys. Rev. B 74 (14) (2006), 144109.
[10] Y. Wang, F. Yang, P. Xiao, Glass-like thermal conductivities in $(La_{1-x1}Y_{x1})_2(Zr_{1-x2}Y_{x2})_2O_{7-x2}$ ($x = x1+x2$, $0<=x<=1$)solid solutions, Acta Mater. 60 (20) (2012) 7024–7033.
[11] X. Ren, C. Wan, M. Zhao, J. Yang, W. Pan, Mechanical and thermal properties of fine-grained quasi-eutectoid $(La_{1-x}Yb_x)_2Zr_2O_7$ ceramics, J. Eur. Ceram. Soc. 35 (11) (2015) 3145–3154.
[12] C. Wan, W. Zhang, Y. Wang, Z. Qu, A. Du, R. Wu, W. Pan, Glass-like thermal conductivity in ytterbium-doped lanthanum zirconate pyrochlore, Acta Mater. 58 (18) (2010) 6166–6172.
[13] Y. Wang, F. Yang, P. Xiao, Rattlers or oxygen vacancies: determinant of high temperature plateau thermal conductivity in doped pyrochlores, Appl. Phys. Lett. 102 (14) (2013).
[14] Y. Wang, F. Yang, P. Xiao, Role and determining factor of substitutional defects on thermal conductivity: a study of $La_2(Zr_{1-x}B_x)_2O_7$ (B = Hf, Ce, $0 \le x \le 0.5$) pyrochlore solid solutions, Acta Mater. 68 (2014) 106–115.
[15] P. Klemens, The scattering of low-frequency lattice waves by static imperfections, Proc. Phys. Soc. 68 (12) (1955) 1113.
[16] B. Abeles, Lattice thermal conductivity of disordered semiconductor alloys at high temperatures, Phys. Rev. 131 (5) (1963) 1906–1911.
[17] L. Minervini, R.W. Grimes, K.E. Sickafus, Disorder in pyrochlore oxides, J. Am. Ceram. Soc. 83 (8) (2000) 1873–1878.
[18] A. Togo, L. Chaput, I. Tanaka, Distributions of phonon lifetimes in Brillouin zones, Phys. Rev. B 91 (9) (2015), 094306.
[19] S. Kasamatsu, T. Tada, S. Watanabe, Theoretical analysis of space charge layer formation at metal/ionic conductor interfaces, Solid State Ionics 183 (1) (2011) 20–25.
[20] B.J. Nyman, M.E. Björketun, G. Wahnström, Substitutional doping and oxygen

vacancies in La2Zr2O7 pyrochlore oxide, Solid State Ionics 189 (1) (2011) 19–28.
[21] M.W. Chase Jr., NIST-JANAF thermochemical tables, J. Phys. Chem. Ref. Data. Monograph 9 (1998).
[22] J.P. Perdew, A. Zunger, Self-interaction correction to density-functional approximations for many-electron systems, Phys. Rev. B 23 (10) (1981) 5048–5079.
[23] J.P. Perdew, K. Burke, M. Ernzerhof, Generalized gradient approximation made simple, Phys. Rev. Lett. 77 (18) (1996) 3865–3868.
[24] S. Grindy, B. Meredig, S. Kirklin, J.E. Saal, C. Wolverton, Approaching chemical accuracy with density functional calculations: diatomic energy corrections, Phys. Rev. B 87 (7) (2013), 075150.
[25] M. Uno, A. Kosuga, M. Okui, K. Horisaka, H. Muta, K. Kurosaki, S. Yamanaka, Photoelectrochemical study of lanthanide zirconium oxides, Ln2Zr2O7 (Ln=La, Ce, Nd and Sm), J. Alloys Compd. 420 (1–2) (2006) 291–297.
[26] S.-i. Tamura, Isotope scattering of dispersive phonons in Ge, Phys. Rev. B 27 (2) (1983) 858–866.
[27] G. Kresse, J. Furthmüller, Efficient iterative schemes for ab initio total-energy calculations using a plane-wave basis set, Phys. Rev. B 54 (16) (1996) 11169.
[28] G. Kresse, J. Hafner, Ab initio molecular dynamics for liquid metals, Phys. Rev. B 47 (1) (1993) 558.
[29] G. Kresse, D. Joubert, From ultrasoft pseudopotentials to the projector augmented-wave method, Phys. Rev. B 59 (3) (1999) 1758–1775.
[30] A.I. Liechtenstein, V.I. Anisimov, J. Zaanen, Density-functional theory and strong interactions: orbital ordering in Mott-Hubbard insulators, Phys. Rev. B 52 (8) (1995) R5467–R5470.
[31] M. Cococcioni, S. de Gironcoli, Linear response approach to the calculation of the effective interaction parameters in the L D A + U method, Phys. Rev. B 71 (3) (2005), 035105.
[32] G. Lan, J. Song, Z. Yang, A linear response approach to determine Hubbard U and its application to evaluate properties of Y_2 B_2 O_7, B = transition metals 3d, 4d and 5d, J. Alloys Compd. 749 (2018) 909–925.
[33] A. Togo, F. Oba, I. Tanaka, First-principles calculations of the ferroelastic transition between rutile-type and Ca Cl_2-type Si O_2 at high pressures, Phys. Rev. B 78 (13) (2008), 134106.
[34] A. Togo, I. Tanaka, First principles phonon calculations in materials science, Scripta Mater. 108 (2015) 1–5.
[35] L. Chaput, A. Togo, I. Tanaka, G. Hug, Phonon-phonon interactions in transition metals, Phys. Rev. B 84 (9) (2011), 094302.
[36] W. Pan, C.L. Wan, Q. Xu, J.D. Wang, Z.X. Qu, Thermal diffusivity of samarium–gadolinium zirconate solid solutions, Thermochim. Acta 455 (1–2) (2007) 16–20.